Welding in the World
https://doi.org/10.1007/s40194-024-01713-9

RESEARCH PAPER

Process comparison of laser deep penetration welding in pure nickel using blue and infrared wavelengths

M. Möbus[1] · R. Pordzik[1] · A. Krämer[1] · T. Mattulat[1]

Received: 26 July 2023 / Accepted: 31 January 2024
© The Author(s) 2024

Abstract

Laser sources with wavelengths in the visible blue spectrum are suitable for heat conduction mode welding of materials like copper and nickel due to the significantly increased Fresnel absorption compared to infrared laser radiation. Recently, blue laser sources with 445 nm wavelength have become available with sufficient power and beam parameters to exceed the intensity threshold for laser deep penetration welding. In laser beam deep penetration welding, the total absorption is significantly increased due to the multiple reflections in the keyhole compared to heat conduction mode welding. However, since the absorbed energy per reflection inside the keyhole is wavelength-dependent, it can be hypothesized that the choice of laser wavelength causes changes in the local energy distribution inside the keyhole, changing the keyhole dynamics. To investigate this, laser beam deep penetration welding experiments were carried out on 2.4068 pure nickel using an infrared laser source and a blue laser source with comparable beam properties. The experiments were monitored and compared by a multi-sensor setup and metallographic analyses. This setup included measurements of airborne acoustic emissions and two high-speed video cameras for spatter tracking and tracking of the keyhole area. The use of a blue laser beam led to a lower spatter quantity, an increase of porosity and a significant change of acoustic emissions, proving the hypothesis for pure nickel.

Keywords Laser beam welding · Nickel · Blue laser source · Absorption · Process stability

1 Introduction

Laser welding can be performed in two different modes, heat conduction welding and deep penetration welding. Heat conduction mode welding occurs when the power density of the laser beam causes the material to melt but is insufficient to vaporize the material and form a so-called keyhole, as it is the case with laser beam deep penetration welding. In both cases, the radiation energy is transferred to the workpiece by Fresnel absorption and plasma reradiation [1]. The Fresnel absorption, besides other influences like the angle of incidence and the temperature, is especially dependent on the wavelength [2]. An infrared laser beam with a wavelength of 1030 nm has an absorption in copper at room temperature of only about 5%, whereas a blue laser beam with a wavelength of 445 nm has an absorption of about 70% [3]. A similar effect, although not as strong, can also be observed for nickel, where the absorption at room temperature increases from about 30% at 1030 nm to approximately 50% at 445 nm [3]. Therefore, a blue wavelength is advantageous especially when it comes to heat conduction mode welding of these materials. In laser deep penetration welding, the laser beam is reflected and absorbed several times by the walls of the keyhole, which considerably increases the overall absorption resulting from the sum of all individual reflections [4], so that absorption efficiencies of over 90% can be achieved, although the Fresnel absorption coefficient is much lower [5]. From this follows, that the smaller the aspect ratio for a given welding geometry, the more advantageous it is to choose a wavelength with a high Fresnel

---

Recommended for publication by Commission IV - Power Beam Processes.

✉ M. Möbus
moebus@bias.de

R. Pordzik
pordzik@bias.de

A. Krämer
kraemer@bias.de

T. Mattulat
mattulat@bias.de

[1] BIAS - Bremer Institut für angewandte Strahltechnik GmbH, Klagenfurter Str. 5, 28359 Bremen, Germany

Published online: 21 February 2024

absorption coefficient in order to maximize the total beam power absorption [4]. Furthermore Fabbro indicates that the use of laser wavelengths which strongly increases the absorptivity of any material decreases the effect of multi-reflections within the keyhole and thus should be an efficient way to easily reduce the range of the operating parameters leading to process instability [6].

Investigations were carried out on the welding of copper with infrared and green laser radiation. It could be shown that, in accordance with [4], the advantages in energy coupling of the green radiation become smaller for deep penetration welding, but there is still a significant difference between the wavelengths in the way of energy coupling in the keyhole, since for the copper materials the green laser radiation forms considerably narrower welds at same weld depth compared to the infrared laser beam [7].

The question how the higher absorption due to a different wavelength influences the laser deep welding process also arose when solid-state laser sources with a wavelength of about 1 µm and sufficient power for deep penetration welding became available after the CO_2-laser sources with a wavelength of 10.6 µm. It was shown that the different absorption properties of solid-state and CO_2 laser wavelengths in steel significantly influence both the energy absorption into the workpiece and the melt pool dynamics [8]. Since the absorbed intensity in steel with perpendicular radiation incidence for the solid-state laser is about 3 times that of the CO_2 laser, the use of high power densities with the solid-state laser consequently results in locally high absorption leading to overheating of the melt and formation of metal vapour [9], spatter [8] and a high dependency on the focusing conditions [10]. The more homogeneous absorption of the laser power compared to the solid-state laser, which is caused by the lower absorbed intensity as well as the smaller gradient depending on the angle of incidence and enhanced by the presence of plasma in the capillary that exhibits high absorption at 10.6 µm and delivers a fraction of the laser power uniformly to the keyhole wall, leads to smoother melt pool dynamics, less spatter formation [8] and a wider parameter range [10].

The state of research shows a clear influence on the keyhole dynamics for the comparison of CO_2 laser sources and solid-state laser sources and their different wavelengths, which, however, cannot be attributed exclusively to the changed Fresnel absorption coefficient due to the plasma absorption. To further clarify the relevant effects, this study aims for a separation of the effects from plasma absorption and a changed Fresnel absorption coefficient onto the keyhole dynamics by using different wavelengths, which both have more comparable plasma absorption behaviours. We investigate the hypothesis that in laser beam deep penetration welding of nickel a change in the laser wavelength from 1030 nm to 445 nm and a resulting increase in the Fresnel absorption coefficient causes changes in the local energy distribution inside the keyhole, changing the keyhole dynamics in terms of fluctuation of the keyhole opening, spatter formation, acoustic emissions and the resulting porosity. To test this hypothesis, bead-on-plate experiments in nickel with both mentioned laser wavelengths were carried out, monitored and compared regarding keyhole dynamics and porosity of the samples by using a multi-sensor setup and metallographic analyses. For this investigation nickel is more expedient than copper, since the Fresnel absorption coefficient also increases considerably from infrared to blue wavelength, but in contrast to laser beam welding of copper, where only unsteady processes can be seen [11], a constant deep penetration welding process is developed. This results in a more comparable welding process. The multi-sensor setup included two high-speed cameras for spatter tracking and tracking of the keyhole area movement accompanied by airborne acoustic emission measurements using an optical microphone which has also been used for monitoring of laser beam processes in other publications [12].

2 Experimental

The experiments were carried out using the disk laser source TruDisk12002 with the optical system BEO D70 (both Trumpf GmbH + Co. KG) and an infrared wavelength of 1030 nm and the diode laser LDMblue 1500–30 with the optical system OTS-5 (both Laserline GmbH) with a blue wavelength of 445 nm. The fibre core diameter of 600 µm and the 1:1 ratio between the focal length of the collimating lens and the focusing lens were chosen identically for both wavelengths, so that the caustics of the two laser beams are similar, resulting in a focal diameter of 576 µm and a Rayleigh length of 3.35 mm (measured with a MSM + HBHP by Primes GmbH) for the TruDisk12002 laser beam and a focal diameter of 596 µm and a Rayleigh length of 2.69 mm (measured with a FM + by Primes GmbH) for the LDMblue 1500–30 laser beam. Due to the different wavelengths of the laser sources, different systems had to be used to measure the beam caustic, which resulted in different resolutions. The settings and properties of the two laser sources used in this study can be seen in Table 1 and Fig. 1.

To investigate the influence of different Fresnel absorption coefficients, bead-on-plate welding experiments were carried out using 2.4068 nickel as sample material, whose composition is given in Table 2 and which was previously cleaned using ethanol. The size of the specimen and the seam lengths of 45 mm are given in Fig. 2. On a single specimen, each parameter listed in Table 3, where the experimental program is shown, was repeated five times. The specimens were changed after every single welding process, and

Table 1 Constant settings of the laser beams

Manufacturer	Diode laser, Laserline LDMblue 1500–30	Disk laser, Trumpf TruDisk12002
Wavelength	455 nm	1030 nm
Fibre diameter	600 µm	600 µm
Focal length of the collimating lens	200 mm	200 mm
Focal length of the focusing lens	200 mm	200 mm
Measured focal diameter	596 µm	576 µm
Angle of incidence	5°	5°
Measured beam parameter product	33 mm • mrad	25 mm • mrad
Measured Rayleigh length	2.69 mm	3.35 mm

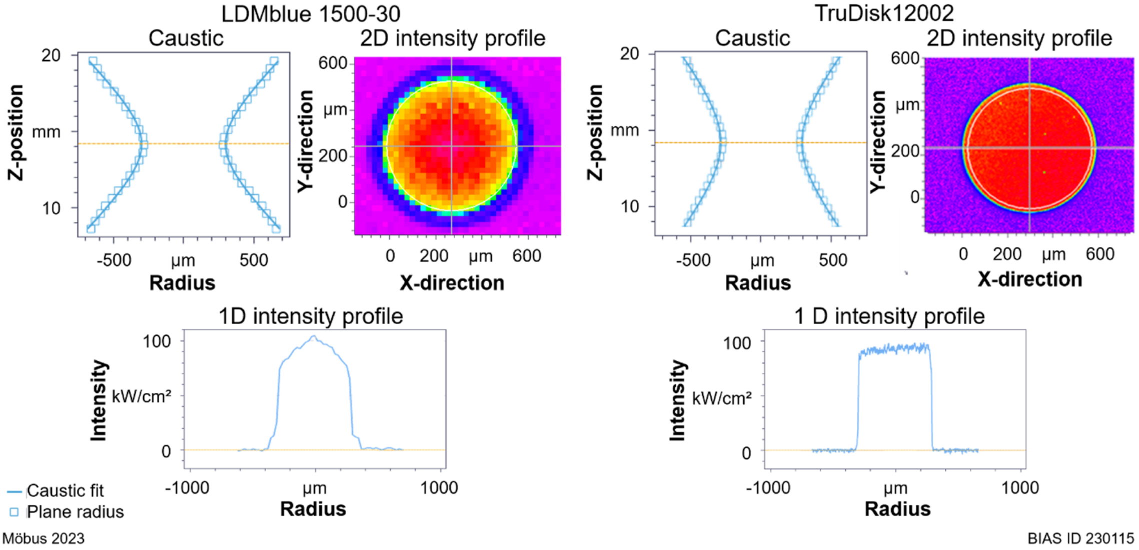

Fig. 1 Measured caustics and one- and two-dimensional intensity profiles in the focal plane of the used laser beams. LDMblue 1500–30 (left) measured with a FM+ (Primes GmbH); TruDisk12002 (right) measured with a MSM+ HBHP (Primes GmbH)

Table 2 Chemical composition of 2.4068 nickel according to [13]

Chemical composition of 2.4068 nickel (wt%)							
Ni	Fe	Co	Mn	C	Cu	Mg	Ti
99.48	0.22	0.02	0.02	0.02	0.01	0.01	0.01

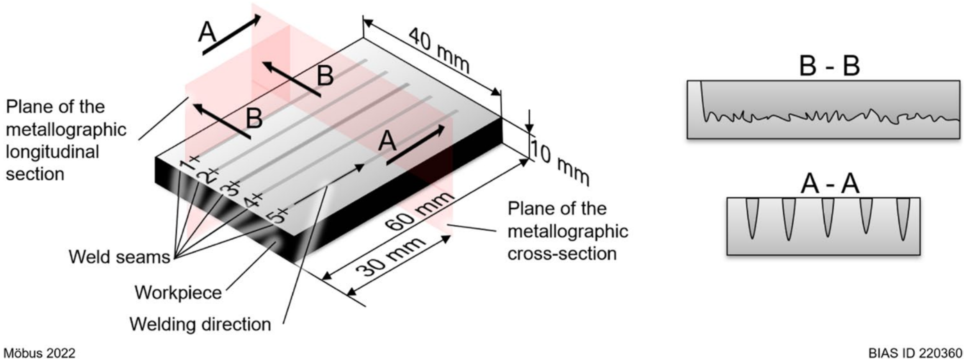
A
B
B
A
40 mm
10 mm
Plane of the metallographic longitudinal section
1
2
3
4
5
Weld seams
Workpiece
Welding direction
60 mm
30 mm
Plane of the metallographic cross-section
B - B
A - A
Möbus 2022
BIAS ID 220360

Fig. 2 Dimensions and design of the specimen (specimen was changed after every single welding process to let the specimen temperature decrease to room temperature before the next weldment)

Table 3 Experimental plan

Material	Laser source	Wavelength (nm)	Focal plane (mm)	Power (W)	Welding speed (m/min)
2.4068 nickel	LDMblue 1500–30	445	0	1340	2.4
2.4068 nickel	LDMblue 1500–30	445	0	1500	2.4
2.4068 nickel	TruDisk12002	1030	0	1400	2.4
2.4068 nickel	TruDisk12002	1030	0	1500	2.4

the specimens cooled down to room temperature and were cleaned by wiping them with a lint-free cloth soaked in ethanol before the next weldment to avoid unwanted effects resulting from pre-heated material or contamination. Cross-sections from the center (cf. Fig. 2 A-A) and longitudinal-sections (cf. Fig. 2 B-B) of each seam were taken and etched by immersion etching for 10 s in a solution of 75 ml water, 75 ml hydrochloric acid and 12.5 g copper sulfate. The metallographic analysis was used to determine the weld penetration depth, the weld penetration depth profile and the porosity on the basis of the mean value and the standard deviation determined from 5 seams each.

Figure 3 shows the experimental welding setup. The welding head was changed from OTS-5 (blue laser source) to BEO D70 (infrared laser source) between the experiments. However, the same crossjet was used, which was also positioned at the same distance from the welding head and the process in order to obtain airborne sound measurements that are comparable. The specimens were placed on a stage for process movement, which provided a constant welding speed of 2.4 m/min. The angle of incidence of the processing setup was tilted by 5° to the vertical orientation against the welding direction, resulting in forehand welding. Argon was used as shielding gas with a flow rate of 15 l/min and a nozzle diameter of 8 mm. All of the sensors described below were mounted on a separate bracket that was not connected to either the stage or the welding head for process movement, so that the positions were not changed when the welding head was changed.

For process monitoring a multi-sensor setup was used, which included measurements of airborne acoustic emissions and two high-speed video cameras for spatter tracking and tracking of the keyhole area.

The high speed camera i-Speed7 (iX Cameras Ltd.) with an AF 180 mm 3.5 Di LD Macro 1:1 SP lens (TAMRON Europe GmbH) and a connected BN810 narrow near-IR bandpass filter was used for spatter tracking with a frame rate of 20 kHz and a resolution of 1064 × 762 pixel (0.007 mm per pixel). It was positioned 90° to the welding direction and in a 0° tilt angle so that an image section of about 7 mm width and 5 mm height around the process zone could be captured. Behind the process zone, a smooth and flat copper mirror was placed which was illuminated by the defocused CAVILUX HF (Cavitar Ltd.) illumination laser in such a way that the radiation falls into the lens of the camera and results in backlight (cf. Fig. 3). This arrangement reduced the visibility of the vapor flares resulting from the welding process and improved the accuracy of the spatter tracking. It was performed using a MATLAB (MATrix LABoratory by MathWorks)-based algorithm, which, after defining the region of interest, creates a binary image using a gray value filter, from which the spatters are identified using the white pixels (cf. Fig. 4). It outputs the spatter velocity

Fig. 3 Left: schematical experimental setup; right: picture of the experimental setup

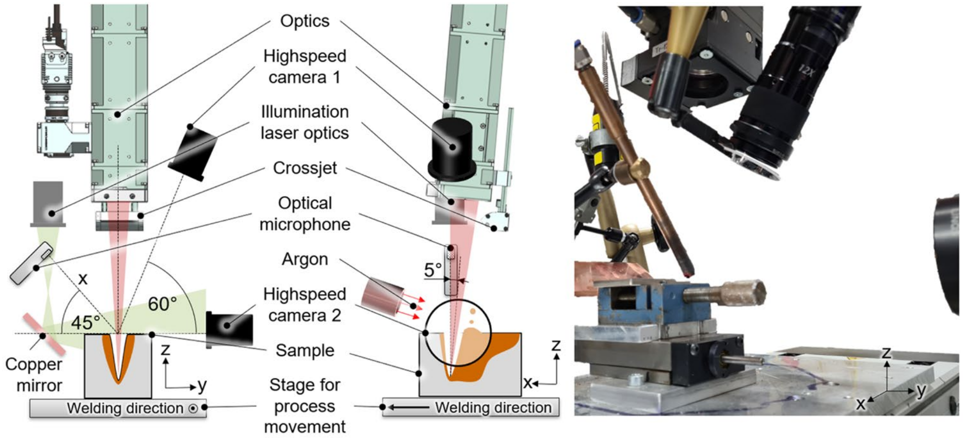

Möbus 2023

BIAS ID 230116

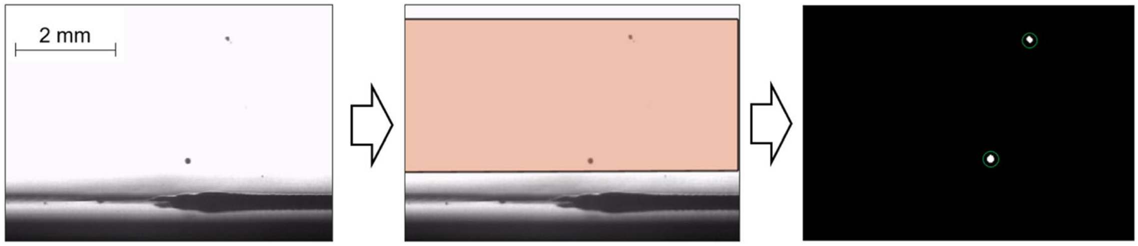

Möbus 2023

BIAS ID 230122

Fig. 4 Left: original frame from a high-speed video used for spatter detection; centre: defined region of interest; right: detected spatter

and direction for each individual spatter as well as the size of the spatter projection in mm^2, which, assuming that the spatters are spherical, can be used to determine the spatter volume. From the average number of spatters per seam multiplied by the average spatter volume, the average spatter quantity per seam in mm^3 was determined, which takes both parameters into account and was also analyzed here. The smallest detectable spatter size depends on the resolution and thus corresponds to a spatter diameter of approximately 0.01 mm.

The keyhole area was tracked by the second high speed camera FASTCAM NOVA S12 (Photron Deutschland GmbH) with a 12× zoom lens system (Navitar, Inc.) and a connected BN810 narrow near-IR bandpass filter operating at a frame rate of 18 kHz and a resolution of 1024 × 944 pixel (0.002 mm per pixel). It was positioned 90° to the welding direction and in a 60° tilt angle so that an image section of about 2.3 mm width and 2.1 mm height around the keyhole opening could be captured. The keyhole area was tracked using a MATLAB-based algorithm that outputs the size of the keyhole area and the keyhole area radius deviation per frame, which was set by means of a brightness threshold, which, however, takes into account not only the keyhole opening, but presumably also a part of the molten pool around it (cf. Fig. 5). The radius deviation σ_r is defined as the standard deviation of the difference between the distances from the centre of gravity of the area to the outer edge of the area r_i and the radius of a perfect circle with the same measured keyhole area $\overline{r}$, thus giving a measure of eccentricity (cf. Fig. 5). A keyhole area radius deviation $\sigma_r = 0$ would therefore mean that it forms a perfect circle.

Measurements of airborne acoustic emissions were made with the Eta250 Ultra optical microphone (XARION Laser Acoustics GmbH) in combination with the NI cRIO-9035 and the NI-9222 module (both National Instruments Corp.) with a sampling rate of 500 kHz. The microphone was positioned at an angle of 90° to the welding direction, a tilt angle of 45° and a distance from the process zone of 130 mm. A built-in cutoff filter of 10 Hz was applied. Using a sliding fast Fourier transformation (FFT) with a window size of 2048 µs and an overlap of 256 µs, the acoustic signal was split into 512 discrete frequency bins ranging from 0 kHz to 250 kHz resulting in an acoustic 3D-spectrogram of the laser welding process as can be seen in Figs. 12 and 13. For a detailed analysis of the frequencies excited by the different processes, a power spectral density over the whole recording length was calculated. It describes the power present in the signal as a function of frequency and was determined using Welch's method [14] with a window size of 10 ms and 5 ms overlap. After relevant frequency bands have been determined, for each time step the spectrogram is then integrated over selected ranges of frequency bands yielding acoustic power curves. These describe the total acoustic emission

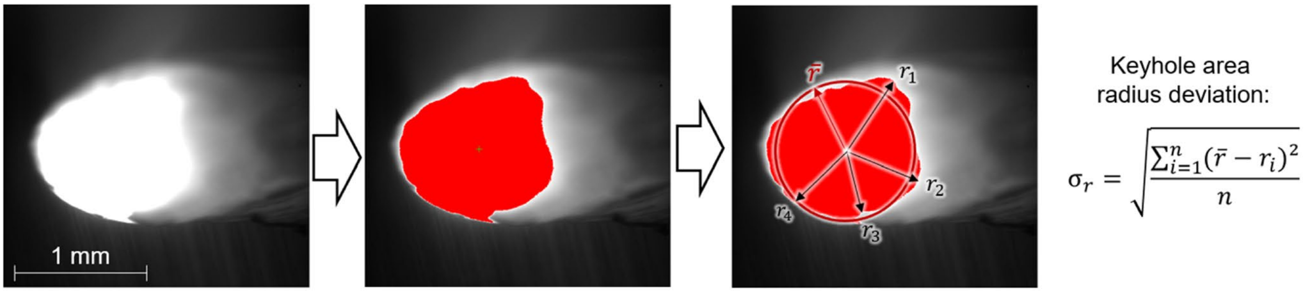
1 mm
$\overline{r}$
r_1
r_2
r_3
r_4
Keyhole area radius deviation:
$\sigma_r = \sqrt{\frac{\sum_{i=1}^{n}(\overline{r}-r_i)^2}{n}}$

Möbus 2023

BIAS ID 230127

Fig. 5 Left: original frame from a high-speed video used for keyhole area measurements; second from left: detected keyhole area; second from right: measured keyhole area; right: definition of the keyhole area radius deviation

in the mentioned frequency ranges over time. In order to negate the effect of the crossjet and other interfering noises like the axis movements, reference recordings where made and subtracted after processing.

The experimental program is shown in Table 3. Two different powers for each laser source were used. The laser beam power of 1400 W for 1030 nm first exceeds the deep penetration welding threshold and the laser beam power of 1500 W for 445 nm corresponds to the maximum power of the LDMblue 1500–30 laser source. The power of the respective other laser source was chosen to reproduce the same weld depths.

3 Results

Figure 6 shows the average weld depth depending on the laser power and the wavelength along with characteristic metallographic cross-sections. It can be seen that the average weld depths and also the seam shapes with lower power (1.23 mm for 445 nm and 1340 W, 1.23 mm for 1030 nm and 1400 W) and with higher power (1.35 mm for 445 nm and 1500 W, 1.35 mm for 1030 nm and 1500 W) are consistent with the other respective experiments. The average seam width of the samples welded with 1030 nm wavelength is slightly higher at lower power than that of the samples welded with 445 nm wavelength (1.24 mm for 445 nm and 1340 W; 1.30 mm for 1030 nm and 1400 W). At higher power (1.37 mm for 445 nm and 1500 W; 1.33 mm for 1030 nm and 1500 W) they are at a comparable level. In the following, the power used is no longer specified, but for simplification only the achieved averaged weld depth.

The weld depth progressions along the length of the seams (cf. Fig. 7) also show no significant differences, whereas the porosity in the sample welded with 445 nm wavelength is significantly higher than in the sample welded with 1030 nm wavelength. This was investigated in more detail in Fig. 8, where the difference in porosity due to wavelength is evident, as the average porosity values of the samples welded by means of blue wavelength (0.68% for $d = 1.23$ mm, 0.98% for $d = 1.35$ mm) exceed those of the samples welded with infrared wavelength (0.21% for $d = 1.23$ mm, 0.19% for $d = 1.35$ mm) by a factor of 3 and 5, respectively. There are no major differences in the shape of the pores, but the average maximum pore feret diameter and the average number of pores (cf. Fig. 9) are also increased for the samples welded with blue wavelength.

The analysis of the spatter tracking shows an increasing average number of spatter per seam (cf. Fig. 10) with increasing weld depth, respectively laser power for both wavelength, whereas the values of the seams welded with infrared wavelength (117 for $d = 1.23$ mm and 297 for $d = 1.35$ mm) are significantly higher than of the seams welded with blue wavelength (52 for $d = 1.23$ mm and 116 for $d = 1.35$ mm). The average spatter amount (which is

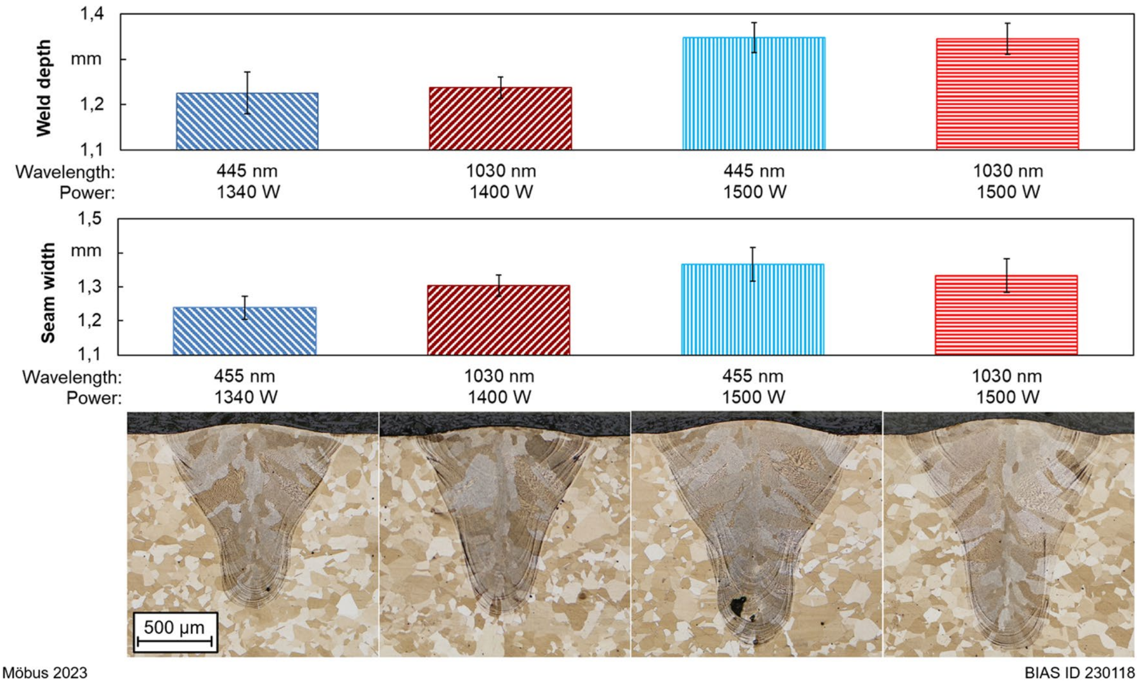

Fig. 6 Average weld depth (top) and average seam width (centre) over laser power and wavelength; characteristic metallographic cross-sections (bottom)

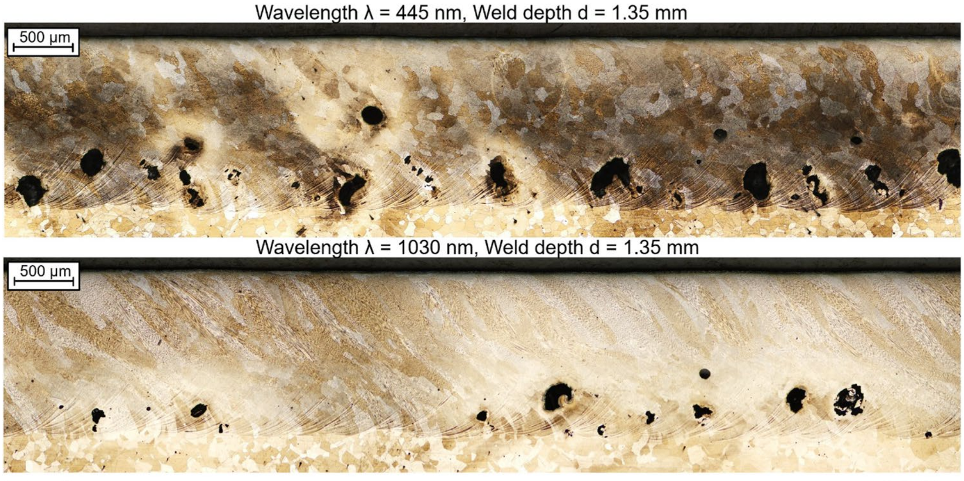
Wavelength λ = 445 nm, Weld depth d = 1.35 mm
500 µm
Wavelength λ = 1030 nm, Weld depth d = 1.35 mm
500 µm

Möbus 2023

BIAS ID 230119

Fig. 7 Etched metallographic longitudinal sections with visible weld depth progression

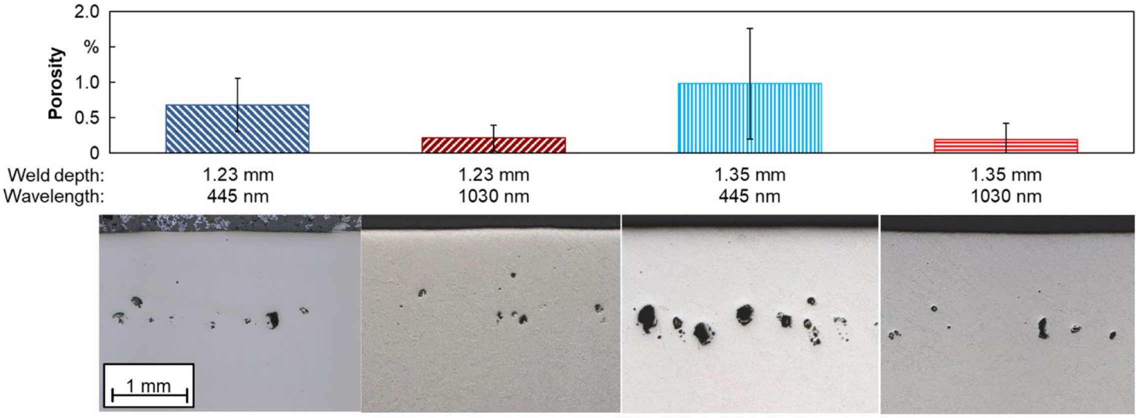

Möbus 2023

BIAS ID 230120

Fig. 8 Porosity over weld depth (laser power) and wavelength (above) and characteristic metallographic longitudinal sections

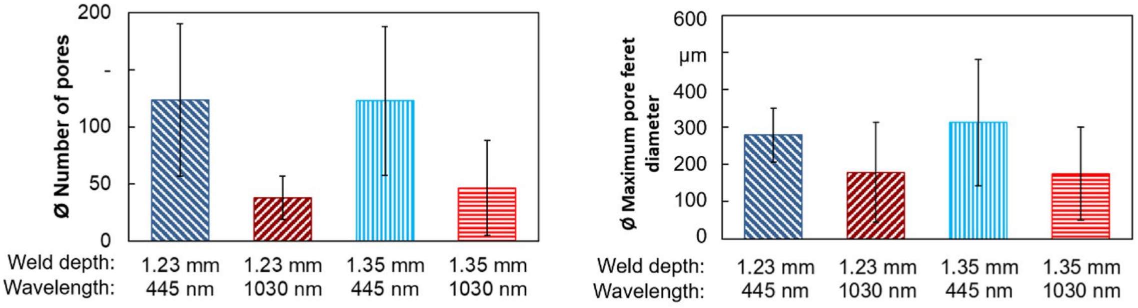

Möbus 2023

BIAS ID 2301128

Fig. 9 Average number of pores (left) and average maximum pore feret diameter (right) over weld depth (laser power) and wavelength

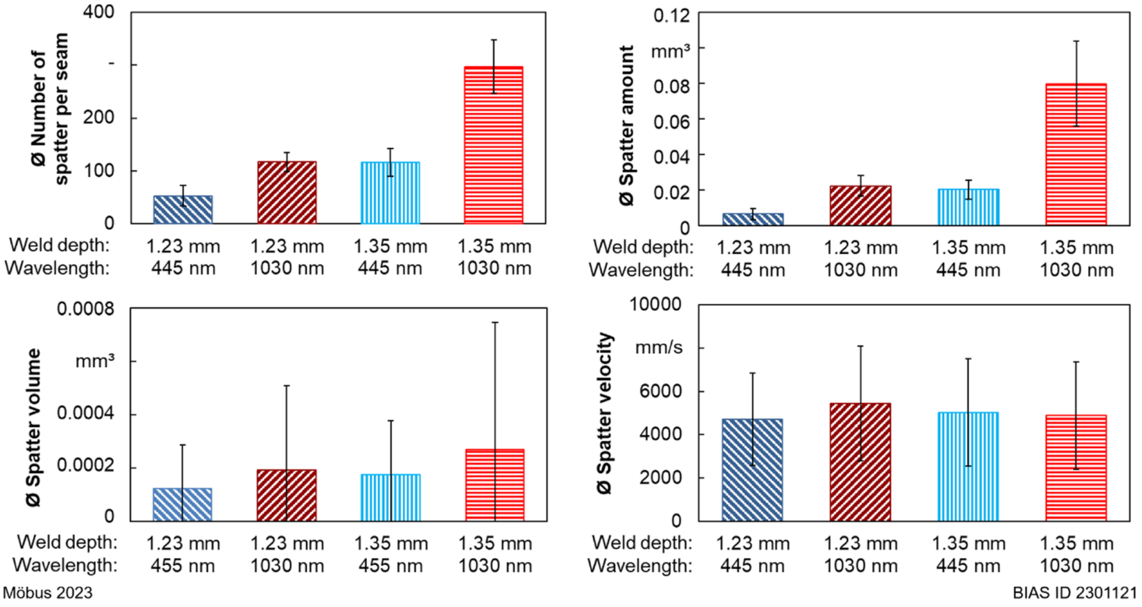

Möbus 2023

BIAS ID 2301121

Fig. 10 Average number of spatter per seam (top left), average spatter volume (bottom left), spatter amount which results from the average number of spatter particles per seam multiplied by the average spatter volume (top right) and average spatter velocity (bottom right), all over weld depth (laser power) and wavelength

defined as the average number of spatter particles per seam multiplied by the average spatter volume) behaves similarly to the average number of spatters, whereas the spatter volumes and the average spatter velocities do not show any significant trends, as their differences lie within the standard deviation.

Fig. 11 shows the results of the keyhole area tracking. It can be seen that the keyhole areas of the samples welded with blue wavelength (0.785 mm^2 for $d = 1.23$ mm and 0.878 mm^2 for $d = 1.35$ mm) are slightly larger than the keyhole areas welded with infrared laser wavlength (0.764 mm^2 for $d = 1.23$ mm and 0.801 mm^2 for $d = 1.35$ mm) and that the keyhole area radius deviations (excentricities) of the samples welded with blue wavelength (58.66 µm for $d = 1.23$ mm and 66.57 µm for $d = 1.35$ mm) are slightly smaller than the keyhole area radius deviations welded with infrared laser wavelength (72.88 µm for $d = 1.23$ mm and 83.57 µm for $d = 1.35$ mm).

Since the welding head needed to be changed when switching from blue to infrared wavelength, it was necessary to check the effect of this change on the microphone signal. Therefore, reference measurements were performed without the welding process, but with crossjet, shielding gas supply, and axis movement in order to visualize possible differences. The results are shown in the spectrograms in Fig. 12. It can be seen that there is a difference in the measurements, and the influences in the setup with the infrared wavelength have a higher dB level. Therefore, in the following PSD and acoustic power analyses, the determined reference data in the form smoothed spectrogram data were subtracted from the

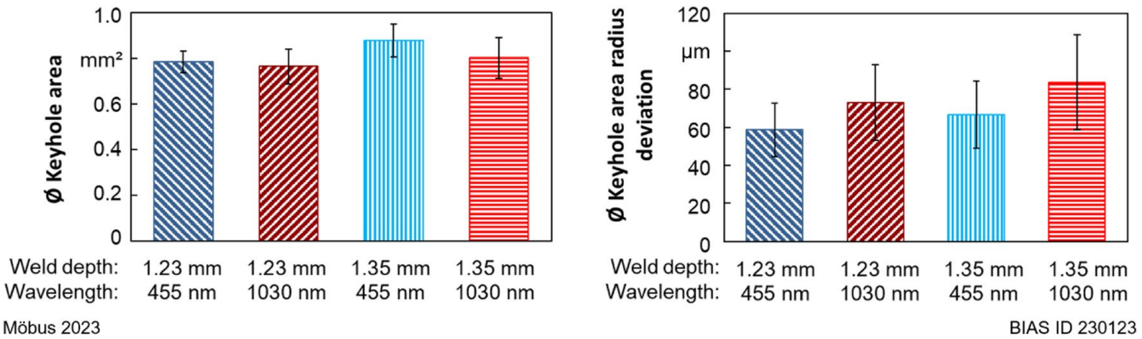

Möbus 2023

BIAS ID 230123

Fig. 11 Average keyhole area (left) and average keyhole area radius deviation (right) over weld depth (laser power) and wavelength

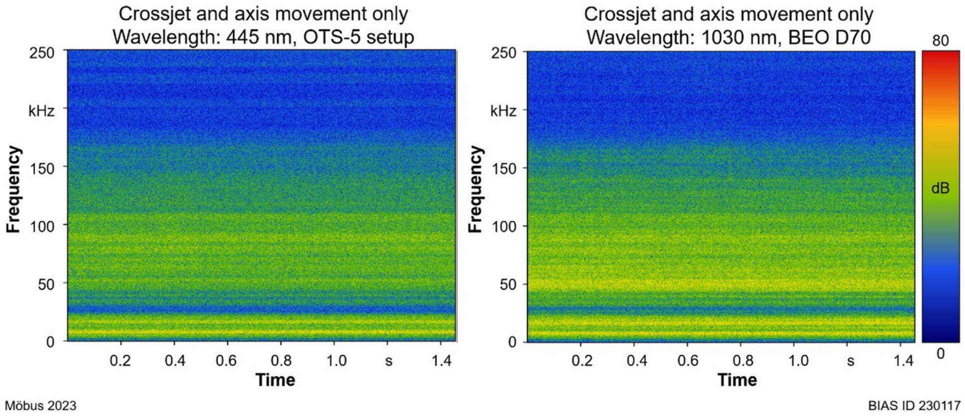

Fig. 12 Reference airborne sound measurement spectrograms of the crossjet and the axis movement only, for the setup with blue wavelength (left) and the setup with infrared wavelength (right)

smoothed spectrogram data recorded with the laser welding process.

Figure 13 shows two characteristic spectrograms of the airborne sound measurement data for the welding process with blue (left) and infrared (right) laser beam wavelength. In this representation, a large difference in the range of about 40 kHz is visible, which will be analyzed in more detail below. Apart from this conspicuity, no other differences become apparent.

The power spectral density (PSD) from 0 kHz to 45 kHz is shown in Fig. 14. Above 45 kHz, no significant acoustic emissions were detected that exceeded those of the crossjet and the axis movement. When looking at the signals produced by welding with the different wavelengths and weld depths, the almost identical progression of the curves is striking. Up to about 15 kHz, only very local differences in the curves can be detected. Beyond, the samples welded with infrared wavelength show a somewhat higher average power spectral density although the progressions of all curves are still very similar. A clear difference between the experiments with blue and with infrared laser wavelength can be observed in the range from about 37 kHz to 42 kHz (cf. range A in Fig. 14), which could also already be seen in Fig. 13. The power spectral density of the tests welded with infrared wavelength increase considerably and thus clearly exceeds the values of the experiments welded with blue wavelength, where the progressions of the curves are also very similar compared to the respective other test welded with the same wavelength. If one compares only the acoustic emissions generated by means of the same wavelength, it is noticeable, especially in the tests with blue wavelength that the higher power and thus the higher welding depth also generated higher acoustic emissions on average. Figure 15 shows on the left side the acoustic power of range A over time and on the right side the average acoustic energy during the welding process. Since Fig. 14 uses a logarithmic scale, and Fig. 15 a linear scale, the higher acoustic power of the processes welded with infrared wavelength ($1.74 \cdot 10^{-6}$ a.u. for $d = 1.23$ mm and $1.99 \cdot 10^{-6}$ a.u. for $\mathrm{d} = 1.35$ mm) in the range from 37 kHz to 42 kHz, compared to the processes with the blue wavelength ($6.8 \cdot 10^{-8}$ a.u. for $d = 1.23$ mm and $1.00 \cdot 10^{-7}$ a.u. for $d = 1.35$ mm) becomes even more significant. The high standard deviation of the tests welded by infrared laser compared to the tests welded with blue wavelength is also striking.

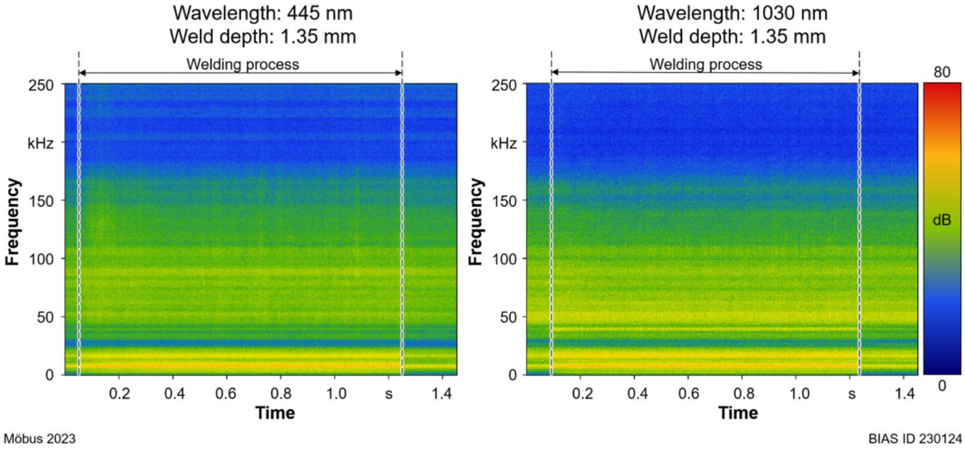

Fig. 13 Characteristic spectrograms of the airborne sound measurement data of the welding process with blue (left) and infrared (right) laser wavelength

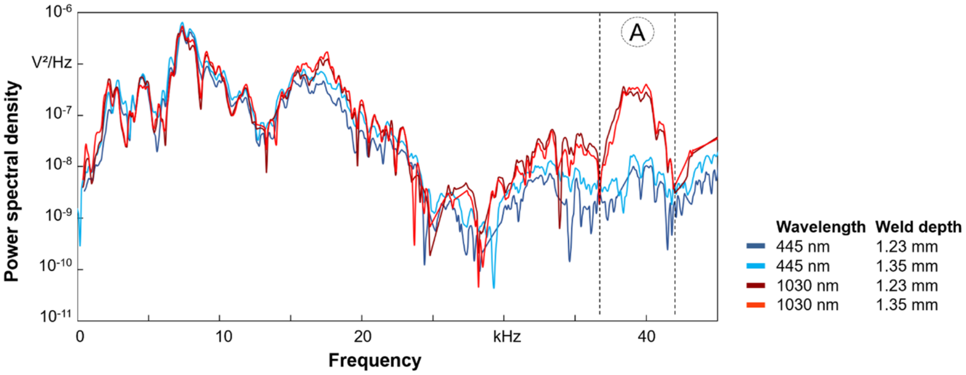

Möbus 2023 BIAS ID 230125

Fig. 14 Power spectral density (PSD) and a specific range A (analysed in the following) of the laser welding process with subtracted crossjet and axis movement emission, over weld depth (laser power) and wavelength

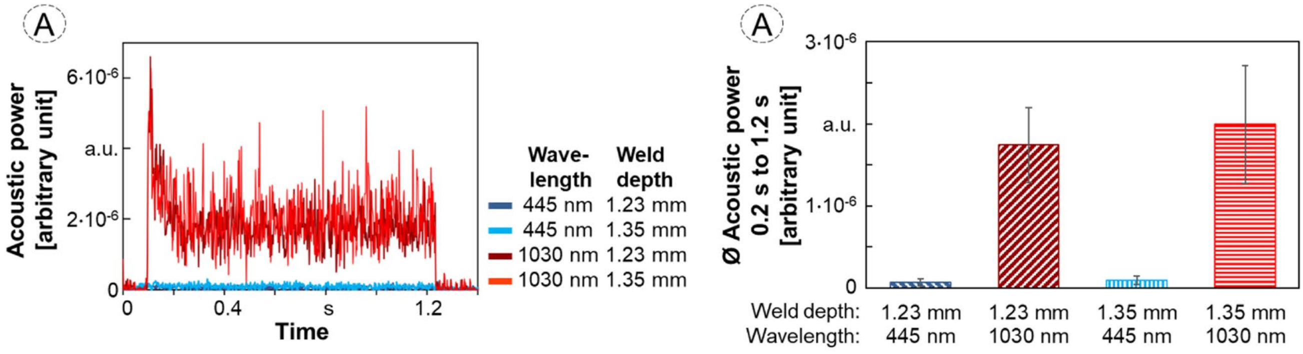

Möbus 2023 BIAS ID 230126

Fig. 15 Acoustic power (left) and average acoustic power (right) as arbitrary units (a.u.) over the significant range A from Fig. 14 over weld depth (laser power) and wavelength

4 Discussion

In the following discussion, the hypothesis that in laser deep penetration welding of nickel, a change in the laser wavelength from 445 nm to 1030 nm and a resulting increase in Fresnel absorption changes in the local energy distribution inside the keyhole, changing the keyhole dynamics in terms of fluctuation of the keyhole opening, spatter formation, acoustic emissions and the resulting porosity is evaluated.

Looking at the dependency between the penetration depths and the wavelengths and laser beam power, it becomes apparent that despite the increase in Fresnel absorption coefficient by factor 1.6 (30% at 445 nm to 50% at 1030 nm), the same weld depths are achieved by very similar laser power. A 1.23-mm-deep weld seam requires about 4% (1400 W at 1030 nm; 1340 W at 445 nm) less laser beam power despite the significant difference in the Fresnel absorption coefficient. To achieve a weld depth of 1.35 mm, the same power of 1500 W is required for blue and infrared wavelengths. This is in good agreement with the literature which states that the influence of the higher Fresnel absorption on the total degree of energy coupling decreases with increasing aspect ratio [4]. Since the weld pool does not change in shape or size at the same laser beam power of 1500 W and welding depth of 1.35 mm, this indicates that the total energy input in the keyhole was the same amount for the blue and infrared wavelengths.

Although the constant keyhole opening and weld depth initially suggest a high process stability, the porosity in the samples welded with blue wavelength exceed those of the samples welded with infrared wavelength by more than three times (cf. Fig. 8), confirming the hypothesis that the increase in Fresnel absorption causes changes in the porosity, since all other process parameters except the wavelength are similar or negligible. There is a difference in the intensity profiles (cf. Fig. 1), since the blue laser beam profile resembles a Gaussian beam profile and the infrared beam profile resembles a Top Hat beam profile. The samples welded with the blue laser at 1500 W should have a higher weld penetration depth due to an influential Gaussian profile with higher peak intensity compared to the intensity of the Top Hat profile at the same power. Furthermore, a higher porosity is more likely to be caused by a Top Hat than by a Gaussian beam profile [15]. Since neither is the case here, the different intensity profiles are probably as negligible, as the slightly different Rayleigh length, the minimum of which (2.69 mm) is well above the maximum weld depth (1.35 mm). Regarding the increased porosity, it can only be assumed at this time that the higher Fresnel absorption causes a larger absorption of the laser beam during initial impact on the keyhole wall, which leads to overheating of the melt and results in a higher vapour pressure [9]. Because of the forehand welding, the laser beam tends to be directed towards the keyhole front rather than the keyhole bottom. The vapour pressure would then hit the keyhole back wall and cause a bulge which may be responsible for the porosity [16]. This theory is to be tested by changing the angle of incidence of the welding head in future experiments.

Surprisingly, the high porosity is associated with lower spatter advent. For the samples welded with blue laser wavelength, a significantly reduced spatter quantity and thus a significantly reduced material loss was measured (Fig. 10), which also confirms the hypothesis. This argues for higher keyhole dynamics when welding with infrared wavelength and therefore reduced Fresnel absorption, which also supports the hypothesis of Fabbro [6] that the higher absorption can increase the process stability in terms of spatter formation. The increased process instability is also indicated by the slightly increased keyhole area radius deviation (eccentricity) in the infrared wavelength experiments, although the difference, as well as the average size of the keyhole area (cf. Fig. 11), is not significant. The hypothesis that the pores are not caused by a constriction of the keyhole as a result of a keyhole collapse but by the bulging of the capillary in the lower region is also supported, since this would otherwise occur in conjunction with increased spattering and an increased keyhole area radius deviation.

The airborne sound analysis initially shows, except for the range A from about 37 kHz to 42 kHz, a very similar pattern over the investigated frequency range (cf. Fig. 13 and Fig. 14) and only very local differences which need to be analysed in the future to determine their origins. The fact that the higher powers and thus the higher welding depths have led to the increased acoustic emissions is in good agreement with [17], where this relationship was investigated. In the mentioned range A, the acoustic power as well as its standard deviation of the tests welded by means of infrared wavelength is increased by more than 10 times, which also speaks for higher process dynamics due to the infrared wavelength. Whether this is related to the spatter will be clarified in the future. Above 45 kHz, however, no relevant acoustic emissions can be detected.

The results of this study show that the change of the laser wavelength influences the keyhole dynamics. Further research is needed to identify the underlying mechanisms of the spatter- and porosity formation with different Fresnel absorption coefficients. The airborne sound analysis also revealed clear differences between the welding processes, but for a comprehensive understanding and an industrial application as a process monitoring system, the fundamental causes of the dissimilar signals need to be investigated further.

5 Conclusion

In this study, laser beam deep penetration welding tests were carried out on 2.4068 pure nickel using a 1030 nm infrared laser beam source and a 445 nm blue laser beam source with comparable beam properties. In each case, two different laser powers that led to the same weld depths compared to the samples welded with the respective other wavelength were used to investigate the hypothesis that a change of the laser wavelength changes the local energy distribution inside the keyhole and the keyhole dynamics in terms of fluctuation of the keyhole opening, spatter formation, acoustic emissions and the resulting porosity. The experiments were monitored and compared by metallographic analyses and a multi-sensor setup including spatter tracking, keyhole area tracking and airborne acoustic emission measurements and the results confirmed the hypothesis.

Five conclusions can be drawn:

1. The change of the laser wavelength from 1030 nm to 445 nm changes the laser beam deep penetration welding keyhole dynamics for pure nickel.
2. The influence of the Fresnel absorption coefficient on the weld penetration depth decreases as the aspect ratio increases for welding pure nickel when changing the laser beam wavelength from infrared to blue.
3. The porosity of the weld seam in nickel can be decreased by the use of an infrared laser beam wavelength with a decreased Fresnel absorption coefficient compared to a blue laser beam wavelength.
4. For laser beam deep penetration welding of nickel, the amount of spatter is reduced and the process stability can be increased compared to a welding process with infrared laser beam wavelength by using a blue wavelength with an increased Fresnel absorption coefficient.
5. By means of airborne sound analysis, clear differences can be detected between the welding of nickel with blue and with infrared wavelength.

Acknowledgements The responsibility for the content of this publication lies with the authors.

Funding Open Access funding enabled and organized by Projekt DEAL.

Data availability Data sets generated during the current study are available from the corresponding author on reasonable request.

Declarations

Conflict of interest The authors declare no competing interests.

Open Access This article is licensed under a Creative Commons Attribution 4.0 International License, which permits use, sharing, adaptation, distribution and reproduction in any medium or format, as long as you give appropriate credit to the original author(s) and the source, provide a link to the Creative Commons licence, and indicate if changes were made. The images or other third party material in this article are included in the article's Creative Commons licence, unless indicated otherwise in a credit line to the material. If material is not included in the article's Creative Commons licence and your intended use is not permitted by statutory regulation or exceeds the permitted use, you will need to obtain permission directly from the copyright holder. To view a copy of this licence, visit http://creativecommons.org/licenses/by/4.0/.

References

1. Steen WM (1991) Laser material processing, 1st edn. Springer, London
2. Johnson P, Christy R (1974) Optical constants of transition metals: Ti, V, Cr, Mn, Fe Co, Ni, and Pd. Phys Rev B 9:5056–5070
3. Spisz EW, Weigand AJ, Bowman RL, Jack JR (1969) Solar absorptances and spectral reflectances of 12 metals for temperatures ranging from 300 to 500/sup 0/K. United States. N. p., NASA-TN-D-5353
4. Dausinger F (1995) Strahlwerkzeug Laser: energieeinkopplung und prozesseffektivität, universität stuttgart, habilitation, stuttgart: Teubner (Laser in der Materialbearbeitung)
5. Kawahito Y, Matsumoto N, Abe Y, Katayama S (2011) Relationship of laser absorption to keyhole behavior in high power fiber laser welding of stainless steel and aluminum alloy. In: J Mater Process Technol 211(10):1563–1568
6. Fabbro R (2020) Depth dependence and keyhole stability at threshold, for different laser welding regimes. In: Appl Sci 10(4):1487
7. Engler S, Ramsayer R, Poprawe R (2011) Process studies on laser welding of copper with brilliant green and infrared lasers. Phys Procedia 12:339–346
8. Rominger V, Schäfer P, Weber R, Graf T (2010) Prozessuntersuchungen beim Laserstrahltiefschweißen – Festkörperlaser hoher Brillanz im Vergleich zu CO2-Lasern. In: DVS reports 267:188–193
9. Körber C (1996) Simultanschweißen – eine Verfahrensvariante zum Schweißen von Grobblechen mit CO2-Laserstrahlung. Dissertation; Berichte aus der Lasertechnik, Aachen
10. Rominger V (2011) High-performance laser welding. In: Laser Technik J 8(3)32–35
11. Maina M, Okamoto Y, Inoue R, Nakashiba S-I, Okada A, Sakagawa T (2018) Influence of surface state in micro-welding of copper by Nd:YAG laser. In: Appl Sci 8(12):2364
12. Sommerhuber R, Kettner M (2022) Monitoring of remote laser processes using air-coupled ultrasound. In: Proceedings of the 12th CIRP conference on photonic technologies [LANE]
13. ATI Flat rolled products: certificate of test according to DIN EN 10204–3.1 - ATI 200/201 NICKEL. (2018)
14. Welch P (1967) The use of fast Fourier transform for the estimation of power spectra: a method based on time averaging over short, modified periodograms. In: IEEE Trans Audio Electroacoustics 15(2):70–73
15. Volpp J (2017) Keyhole stability during laser welding—part II: process pores and spatters. In: Production Engineering 11(1):9–18
16. Boley M, Berger P, Webster PJL, Weber R, van Vlack C, Fraser J, Graf T (2013) Investigating the weld depth behaviour using different observation techniques: X-ray, inline coherent imageing and highspeed observation during welding ice. ICALEO® 2013: 32nd International congress on laser materials processing, laser microprocessing and nanomanufacturing; October 6–10, 2013; Miami, Florida, USA; In: International congress on applications of lasers & electro-optics; Laser Institute of America, pp 22–27
17. Tomcic L, Ederer A, Grabmann S, Kick M, Kriegler J, Zaeh MF (2022) Interpreting acoustic emissions to determine the weld depth during laser beam welding. In: J Laser Appl 34(4):42052

Publisher's Note Springer Nature remains neutral with regard to jurisdictional claims in published maps and institutional affiliations.